PHYSICAL REVIEW MATERIALS **7**, 085002 (2023)

Comparative study of physical properties of $Ti_{50-x}Ni_{48+x}Fe_2$ ($x = 0.0-2.0$) shape memory alloys after solution treating and aging at 450 °C

Pallab Bag,[1] Yu Sian Lee,[1] Jing-Yue Chen,[1] Yung-Kang Kuo,[1,*] and Shyi-Kaan Wu[2]
[1]*Department of Physics, National Dong Hwa University, Hualien 97401, Taiwan*
[2]*Department of Materials Science and Engineering, National Taiwan University, Taipei 10617, Taiwan*

(Received 1 May 2023; accepted 31 July 2023; published 22 August 2023)

We report a comprehensive study of the physical properties of two series of $Ti_{50-x}Ni_{48+x}Fe_2$ ($x = 0.0 - 2.0$) alloys synthesized after solution treated and aged at 450 °C using temperature (T)-dependent electrical resistivity (ρ), Seebeck coefficient (S), specific heat (C_p), and thermal conductivity (κ) measurements. All measured physical properties indicated that point defects with Ni addition altered martensitic transformation (MT) characteristics from two-stage $B2 \leftrightarrow R \leftrightarrow B19'$ to strain-glass (STG) type in solution-treated alloys, whereas precipitation of Ti_3Ni_4 with excess Ni in aged alloys exhibited another R-phase transition. These alloys exhibit metallic behavior in $\rho(T)$ and $S(T)$; however, their electrical properties vary significantly with increasing x, due to the increase in point defects and precipitates. Despite this, solution-treated alloys with $x \geqslant 1.0$ exhibit a negative temperature coefficient of resistivity below the STG phase due to their continuous formation and growth of R domains. The scattering of charge carriers for both series of alloys in the $B2$ phase appears to be composition independent, although the electronic band structure near Fermi levels varies considerably at each MT. An analysis of $\kappa(T)$ data reveals that charge carriers contribute more to the MT features than phonons. As Ni content increases, electron-phonon coupling weakens, and phonon modes become harder in these alloys. Furthermore, the entropy change associated with the two intermediate R-phase MTs induced by point defects and Ti_3Ni_4 precipitates is estimated using $C_p(T)$, which decreases with lowering transition temperatures and can be explained by theoretical ferroelastic models.

DOI: 10.1103/PhysRevMaterials.7.085002

I. INTRODUCTION

TiNi-based shape memory alloys (SMAs) have received extensive research attention in condensed-matter physics and materials science divisions owing to their exceptional functional and mechanical properties, including good mechanical properties, excellent memory power, pseudoelasticity, high damping capacity, low elastic anisotropy, high corrosion/abrasion resistance, and giant elastocaloric effect [1–6]. Materials with such multifunctional properties are widely used in automotive, aerospace, electronics, mechanical engineering, and medical science applications such as actuators, robotics, antennas, couplings, orthodontic wire, guide wire, and stents [4–9]. Stoichiometric TiNi alloy usually exhibits a first-order thermoelastic displacive and diffusionless martensitic phase transition (MT) from high-temperature austenite cubic $B2$ phase (CsCl-type structure with $Pm3m$ space group) to the low-temperature martensite monoclinic $B19'$ phase (space group: $P2_1/m$) near room temperature with an utmost lattice distortion of about 10% [4,8]. The martensitic state in SMAs is a long-range strain-ordered ferroelastic state, analogous to the ferroelectric and ferromagnetic system where long-range electric dipoles and magnetic moments occur [10,11].

In TiNi-based SMAs, the MT temperature and related characteristics are greatly influenced by point defects, generally introduced by changing the Ni/Ti ratio or by alloying a third element such as Cu, Fe, Mn, Co, Cr, etc. [4,8,12–17]. The MT temperature in TiNi-based SMAs decreases with increasing point defects by globally changing the thermodynamic stability of the martensite phase as well as the development of local frustration. It could be understood in terms of Fermi-surface nesting and the variation of density of states (DOS) near the Fermi level [18–22]. The point defects can also generate abnormal or nonideal strain states in TiNi-based alloys, such as precursors and strain glass (STG) [12–17,23–30]. The precursor state is a special kind of strain state and is also known as the premartensite state (e.g., R and $B19$ phases with a lattice distortion of ~1 and 8%, respectively), in which the strains are not frozen but ergodic [4,15,18,19,30,31]. In contrast, strains are frozen in arbitrary directions in the STG state due to local stresses and the frustrations inhabited by significant point defects [23–27,31,32]. However, there could be a short-range strain ordering in the STG state but no ergodicity. Furthermore, the MT characteristics in TiNi-based SMAs were also sensitive to thermal treatment with precipitates and mechanical treatment of dislocations (cold working) [2,4,8,33–37]. It has been found that intermediate-temperature aging at 200−550 °C with an optimal duration of 25–100 h produces Ti_3Ni_4 precipitates, which have a rhombohedral structure (space group: $R3$) [38–40]. For example, the precipitation of Ti_3Ni_4 in Ni-rich aged TiNi binary SMA leads to

---

[*] ykkuo@mail.ndhu.edu.tw

a phase transition from $B2$ phase to the R phase prior to the $B19'$ martensite phase [41,42]. Further, the Ti_3Ni_4 precipitates in Ni-rich $Ti_{48.7}Ni_{51.3}$ SMA alter the MT characteristics from the STG phase in solution treated to the R phase due to the thermal aging [36,39,43].

The Fe-doped TiNi SMAs are especially intriguing due to their diverse MT characteristics with Fe concentrations [4,13,17,28–30]. A generic phase diagram of $Ti_{50}Ni_{50-x}Fe_x$ SMAs reveals that Fe doping changes the MT sequence to a two-step type ($B2 \leftrightarrow R \leftrightarrow B19'$) for $x = 3\%$ Fe. While a one-step $B2 \leftrightarrow R$ MT was observed in the $3 < x < 5$ range and for $x \geqslant 6\%$, the MT characteristics are STG type [17,29,30]. The intermediate R phase in Fe-substituted TiNi alloys is a trigonal structure with a $P3$ space group, and most likely arises to a drastic change in atomic-scale local lattice distortion with Fe substitutions [4,17,30]. This R phase appears when the hardening of phonon modes in the $B2$ phase occurs, which is inhabited by the Fermi-surface nesting with point defects [17,19,44]. The STG phase, on the other hand, appears when the excessive point defects are present in the $Ti_{50}Ni_{50-x}Fe_x$ alloys, where local energy barriers between the austenite ($B2$) and martensite (R and $B19'$) phases are almost equal [17,29–31,45]. Recently, a study on the MT characteristics of $Ti_{50-x}Ni_{48+x}Fe_2$ ($x = 0.0 - 2.0$) SMAs using mechanical strain and differential scanning calorimetry (DSC) measurements revealed that increasing point defects with Ni/Ti ratio alter the MT features to STG type for solution-treated alloys, whereas thermally aged alloys at 450 °C undergo another R-phase MT due to Ti_3Ni_4 precipitate formation [46,47]. In this regard, Ni-rich Fe-substituted $Ti_{50-x}Ni_{48+x}Fe_2$ SMAs synthesized using different methods/routes are of particular interest; therefore, a comparative study of their physical properties will be highly beneficial.

In this work, we comprehensively studied the electrical and thermal transport properties of solution treated and 450 °C aged $Ti_{50-x}Ni_{48+x}Fe_2$ SMAs with $x = 0.0–2.0$ using electrical resistivity, Seebeck coefficient, specific heat, and thermal conductivity measurements. These measurements indicated that increased point defects and Ti_3Ni_4 precipitates with increasing Ni/Ti ratios significantly influenced the MT characteristics in two sets of $Ti_{50-x}Ni_{48+x}Fe_2$ alloys. We discuss the scattering of charge carriers across the MTs with the help of $\rho(T)$, $S(T)$, and $\kappa(T)$ measurements. Additionally, the entropy change associated with the MTs is calculated using $C_p(T)$ measurement, and its variation with x can be described by theoretical ferroelastic models. This study represents an assessment of the physical properties of two intermediate R-phase transformations induced by point defects with Ni/Fe substitutions and Ti_3Ni_4 precipitates with thermal aging in TiNi-based alloys.

II. MATERIALS AND METHODS

Polycrystalline samples of $Ti_{50-x}Ni_{48+x}Fe_2$ ($x = 0.0$, 0.5, 1.0, 1.5, and 2.0) SMAs were prepared by an arc-melting technique taking the appropriate amounts of the constituent elements. The mixture of the high-purity elements (all purity > 99.9%) was remelted and flipped several times in the arc-melting furnace under a flowing high-purity argon atmosphere to ensure better chemical homogeneity single phase. A high-purity Ti button was used as a gettering element to absorb residual oxygen in the arc-melting furnace chamber. The weight loss of each sample during the remelting process was less than 0.01%. The obtained ingots were then hot rolled at 900 °C into plates with a thickness of about 2 mm using a commercial rolling machine (DBR150 × 200 2HI-MILL, Daito Seiki Co, Japan). In the present study, we used two sets of $Ti_{50-x}Ni_{48+x}Fe_2$ samples to study the electrical and thermal properties. One set of ingots was homogenized at 900 °C for 1 h and subsequently cooled to room temperature by quenching in water, named solution treated. Another set of samples was encapsulated in a vacuum quartz tube and annealed at 450 °C for 100 h, followed by quenching in water, named aged at 450 °C. The same preparation technique has been used in other studies reported elsewhere [17,46,47].

The phase purity and crystal structure of the two sets of prepared samples were reported earlier by x-ray diffraction, scanning electron microscope, and transmission electron microscope techniques at room temperature in Refs. [46,47]. It was revealed that the solution-treated samples have the majority of $B2$ phase and a minority of Ti_2Ni phase associated with oxygen contamination during the process of melting in the furnace. On the other hand, thermally aged samples form Ti_3Ni_4 precipitates in addition to $B2$ and Ti_2Ni phases. However, no precipitates of Ti_3Ni_4 were detected in the aged $Ti_{50}Ni_{48}Fe_2$ sample [46,47].

For the electrical and thermal transport measurements, all sample plates were cut into a rectangular parallelepiped shape with a dimension of approximately $5.0 \times 1.5 \times 1.5\ \mathrm{mm}^3$ using a low-speed diamond-wheel saw cutter. The temperature-dependent electrical resistivity measurement of these samples was carried out in a closed-cycle refrigerator over the temperature range of 10–400 K using the standard four-probe dc method. The Seebeck coefficient and thermal conductivity were measured simultaneously using a homemade apparatus with the direct-heat pulse technique. The specific-heat data for these SMAs were obtained using a high-resolution ac calorimeter with chopped light as a heat source. More details about these characterization techniques can be found elsewhere [17,27,48].

III. EXPERIMENTAL RESULTS

A. Electrical resistivity

The temperature-dependent electrical resistivity $\rho(T)$ in the two set of $Ti_{50-x}Ni_{48+x}Fe_2$ ($x = 0.0 - 2.0$) SMAs was measured during cooling and warming, as shown in Fig. 1. For the sake of clarity, the $\rho(T)$ for all alloys were normalized with respect to the resistivity at 10 K ($\rho_{10\,\mathrm{K}}$), $\rho(T)/\rho_{10\,\mathrm{K}}$. As shown in Fig. 1(a), the $\rho(T)/\rho_{10\,\mathrm{K}}$ of the solution-treated alloys with $x = 0.0$ and 0.5 showed abrupt changes in ρ at the $B2 \leftrightarrow R$ and $R \leftrightarrow B19'$ MTs. The intermediate R phase, in this case (denoted as $R1$), is induced by point defects with Fe substitutions [13,17,30,46,47]. The MT temperatures for the $B2 \leftrightarrow R1$ (T_{R1}) and $R1 \leftrightarrow B19'$ (T_M) of these samples are estimated from the temperature of minima in the $d\rho/dT$ vs T curve and are listed in Table I. Thermal hysteresis (ΔT_H) between cooling and warming of the $\rho(T)$ for the T_{R1} and T_M [see Fig. 1(a)] implies the first-order nature of the martensitic

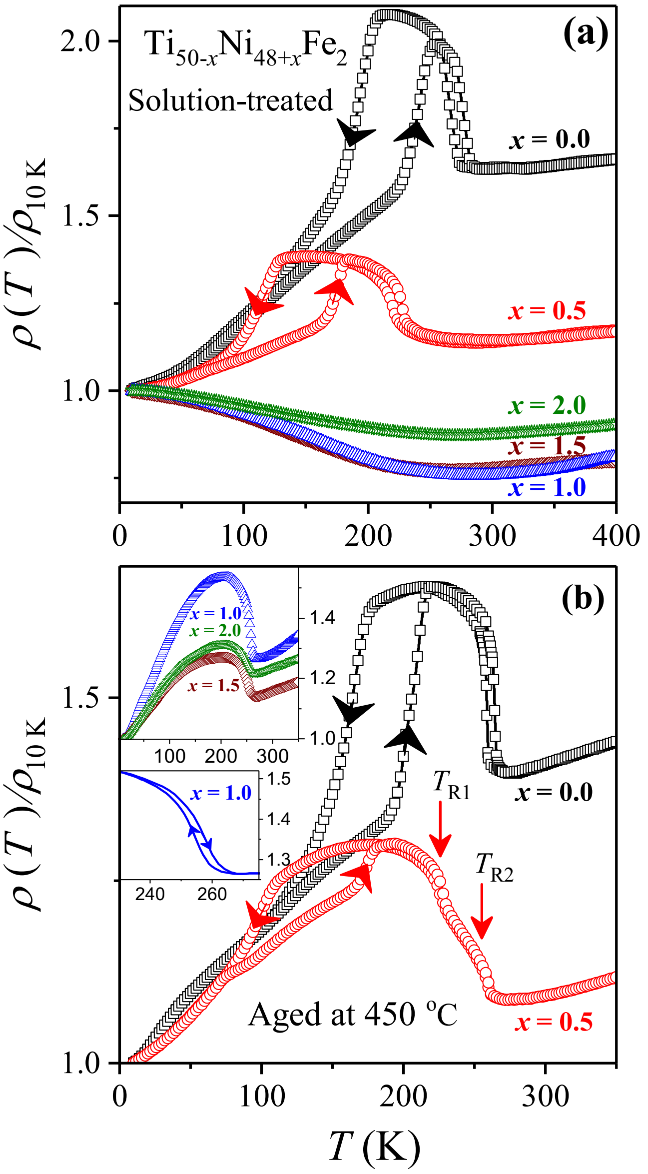

FIG. 1. (a) Temperature dependence of electrical resistivity $\rho(T)$ of solution-treated $Ti_{50-x}Ni_{48+x}Fe_2$ SMAs with $x = 0.0$, 0.5, 1.0, 1.5, and 2.0 during cooling and warming cycles. (b) $\rho(T)$ data for thermally aged $Ti_{50-x}Ni_{48+x}Fe_2$ alloys with $x = 0.0$ and 0.5. Vertical arrows indicate two-stage R-phase transformation (T_{R1} and T_{R2}) for the $x = 0.5$ sample. Upper inset shows $\rho(T)$ data for alloys with $x = 1.0$, 1.5, and 2.0, and lower inset shows thermal hysteresis between cooling and warming across T_{R2} for $x = 1.0$.

phase transition. It also appears that T_{R1} and T_M values for the $x = 0.5$ sample are lower than the $x = 0.0$ sample, suggesting that point defects with Ni doping lower the driving force for MTs, consistent with previous studies on doped TiNi-based alloys [15–17,27,31]. In contrast, the characteristics of MT for $x \geqslant 1.0$ showed STG behavior. The $\rho(T)/\rho_{10\,K}$ of $x = 1.0$, 1.5, and 2.0 samples demonstrated a positive temperature coefficient of resistivity (TCR) > 250 K and negative TCR < 200 K [see Fig. 1(a)], similar to the STG phases observed in $Ti_{50}Ni_{50-x}Fe_x$ alloys for $x \geqslant 6$ and Ni-rich $Ti_{50-x}Ni_{44+x}Fe_6$ alloys [13,17]. However, it differed from the negative TCR observation over a wide temperature range from 300 to 10 K in Ni-rich $Ti_{50-x}Ni_{50+x}$ alloys with $x \geqslant 1.3$ [16,27]. The STG transition temperatures (T_G), estimated as the inflection point of the $d\rho/dT(T)$ curve, are listed in Table I. It was noticed that the T_G of these alloys was much lower than that of the Ni-rich $Ni_{50-x}Ti_{50+x}$ SMAs with $x \geqslant 1.3$ (T_G > 175 K) [16,27].

Figure 1(b) represents the $\rho(T)/\rho_{10\,K}$ of aged $Ti_{50-x}Ni_{48+x}Fe_2$ SMAs, showing similar two-step MT characteristics in the $x = 0.0$ sample; however, MTs become three stages for the $x = 0.5$ sample. Upon warming, $\rho(T)/\rho_{10\,K}$ of the $x = 0.5$ sample showed anomalous behavior in ρ at 174.5 K due to the $B19'$ transformation and two successive steplike changes in ρ above 200 K (indicated by arrows). This finding was consistent with the previous DSC measurements on the same composition and thermal-aging treatment, indicating that it undergoes two successive intermediate R-phase transformations [46,47]. One R-phase transformation ($R1$) occurs at $T_{R1} \simeq 228$ K due to point defects induced by Fe/Ni substitution, and another R-phase transformation (denoted as $R2$) occurs at $T_{R2} \simeq 260$ K due to the formation of Ti_3Ni_4 precipitates [46,47]. A similar type of T_{R2} transformation has also been observed in many TiNi-based alloys after thermal aging [36,41,42]. In contrast, $\rho(T)/\rho_{10\,K}$ of the aged samples with $x = 1.0–2.0$ displayed changes in ρ due to T_{R2} only [see upper inset of Fig. 1(b)] [46,47]. The ΔT_H between cooling and warming was observed at T_{R2} for these alloys, e.g., $\Delta T_H \simeq 3.4$ K for $x = 1.0$ sample [see lower inset of Fig. 1(b)]. No anomalies were found for the $R1$ and $B19'$ phases or STG-like phases in $\rho(T)$ at low temperatures, significantly different from those obtained in the same Ni-doped solution-treated series. In Fig. 1(b), a small ΔT_H value (< 6.0 K) is observed for T_{R1} and T_{R2}, while a large ΔT_H is observed for T_M (> 40 K). Table II summarizes the MT temperatures (T_{R1}, T_{R2}, and T_M) of the aged samples. It indicates that the T_{R1} and T_M values of the aged alloys differ slightly from those of the solution-treated alloys, possibly due to compositional variation of Ti, Ni, and Fe in the TiNi matrix [36,46,47]. Besides, T_{R2} values also decreased with Ni content, a phenomenon related to the size and distribution of precipitates in the matrix [36,46,47]. All the variations in MT temperatures with increasing Ni/Ti ratios will be discussed further in Sec. IV, Discussion.

The $\rho(T)$ of both series of alloys for below and above the MTs regions showed positive TCR characteristics, indicating a metal-like behavior. However, the solution-treated samples with $x = 1.0–2.0$ displayed a negative TCR at low temperatures in the STG phase. We found that the residual resistivity at 10 K ($\rho_{10\,K}$) in the solution-treated samples was about 52 and 71 μΩ cm for $x = 0.0$ and 0.5 samples, respectively, while $\rho_{10\,K}$ values for $x = 1.0–2.0$ samples were relatively higher in the range of 120–160 μΩ cm. On the other hand, the $\rho_{10\,K}$ values for aged samples increased from ~55 μΩ cm for $x = 0.0$ to ~110 μΩ cm for $x = 1.0$, then decreased to ~74 μΩ cm for $x = 2.0$. The residual resistivity ratio (RRR) at 300 K, i.e., $\rho_{300\,K}/\rho_{10\,K}$, was about 1.64 and 1.14 for the $x = 0.0$ and 0.5 solution-treated samples, respectively, while the RRR values for the $x = 1.0–2.0$ samples were less than 1.0 (see Table I). The RRR value for the aged samples with $x = 0.0$ was about 1.41, while the RRR values for the other

TABLE I. Deduced values of MT characteristic temperatures (T_{R1}, T_M, and T_G) from $\rho(T)$, $S(T)$, and $\kappa(T)$ data, residual resistivity ratio (RRR) at 300 K, Fermi energy (E_F) in $B2$-phase, ratio of electronic to lattice thermal conductivity (κ_e/κ_L) at 300 K, and entropy change (ΔS) at T_{R1} for solution-treated $Ti_{50-x}Ni_{48+x}Fe_2$ ($x = 0.0 - 2.0$) alloys.

Solution-treated alloys	MT temperatures (K) from $\rho(T)$			RRR	MT temperatures (K) from $S(T)$		E_F (eV)	MT temperatures (K) from $\kappa(T)$		κ_e/κ_L ratio	ΔS (J/mol K) at T_{R1}
	T_{R1}	T_M	T_G		T_{R1}	T_M		T_{R1}	T_M		
0.0	276.6	241.8		1.64	276.2	244.5	2.0	274.0	246.8	1.9	1.76
0.5	227.4	176.6		1.14	227.9	178.5	2.2	226.9	178.8	2.9	1.20
1.0			164.5	0.76			2.1			1.5	
1.5			148.4	0.76			2.3			1.0	
2.0			117.2	0.87			1.8			0.9	

samples lay between 1.1 and 1.3 (see Table II). It suggests that point defects with increasing Ni/Ti ratios and the Ti_3Ni_4 precipitates with thermal aging degrade the metallic properties of $Ti_{50-x}Ni_{48+x}Fe_2$ SMAs.

B. Seebeck coefficient

To further explore the electrical transport properties in both series of Ni-rich $Ti_{50-x}Ni_{48+x}Fe_2$ SMAs, we carried out the Seebeck coefficient measurements in the temperature range of 10–400 K. The Seebeck coefficient is a highly sensitive probe for the phenomena like electronic band structure near the Fermi level and the changes in the position of Fermi energy (E_F) across the density of states of a material. Furthermore, previous studies have demonstrated that the Seebeck coefficient is a more sensitive probe to determine the MT temperature of TiNi-based SMAs [17,27,49]. Figure 2 shows the temperature-dependent Seebeck coefficient $S(T)$ of both series of synthesized $Ti_{50-x}Ni_{48+x}Fe_2$ ($x = 0.0$–2.0) SMAs. The sign of S for all these samples in the present study was positive in the entire temperature range of interest, indicating that the holes were the dominant charge carriers for thermoelectric transport. Furthermore, the hole-type charge carriers in $Ti_{50-x}Ni_{48+x}Fe_2$ SMAs were consistent with the other TiNi-based SMAs, such as $Ti_{50-x}Ni_{50+x}$ and $Ti_{50}Ni_{50-x}Cu_x$ [15,16,27,50].

Figure 2(a) shows the $S(T)$ curves of solution-treated $Ti_{50-x}Ni_{48+x}Fe_2$ alloys during cooling and warming cycles, clearly showing an abrupt jump in S at the two-step MTs (T_{R1} and T_M) for $T > 100$ K with a sizable thermal hysteresis for the samples with $x = 0.0$ and 0.5. In contrast, no discernible changes in slope can be observed for $x = 1.0$–2.0 samples [see the inset of Fig. 2(a)], which is associated with the STG transition. The MT temperatures (T_{R1} and T_M) estimated from $S(T)$ curve (see Table I) are noticeably lower for the $x = 0.5$ sample than for the $x = 0.0$ sample and are well aligned with those obtained from the $\rho(T)$ data. Figure 2(a) also shows that the magnitude of the overall change in S at T_{R1} is much smaller than that at T_M for both samples, indicating that the modulation of the electronic band structure or the change in DOS at the Fermi surface has a larger contribution to the $B19'$-phase transition than the intermediate R-phase transition [15,17,50].

Figure 2(b) shows the $S(T)$ data of 450 °C aged $Ti_{50-x}Ni_{48+x}Fe_2$ alloys with $x = 0.0$ and 0.5 during cooling and warming cycles, showing a similar jumplike S behavior at $R1$- and $B19'$-phase transformation temperatures. In addition, a weak jumplike anomaly at $T_{R2} \simeq 262$ K for the $x = 0.5$ sample [highlighted in the upper inset of Fig. 2(b)] signifies the occurrence of the intermediate R-phase transition due to precipitates, in agreement with the $\rho(T)$ data. On the other hand, a notable jump in S is seen at T_{R2} for $x = 1.0 - 2.0$ aged samples [see lower inset of Fig. 2(b)], suggesting a larger volume fraction of $R2$-phase transformation when the Ni content in $Ti_{50-x}Ni_{48+x}Fe_2$ alloys is higher [46,47]. This can be ascribed to the size and distribution of precipitates in the TiNi-matrix with Ni supersaturation, similar to the Ni-rich $Ti_{48.7}Ni_{51.3}$ SMAs [36,51,52]. The MT temperatures (T_{R1}, T_{R2}, and T_M) of the aged alloys obtained from $S(T)$ data are listed in Table II. In addition, Fig. 2(b) shows that the change in S

TABLE II. Deduced values of MT characteristic temperatures (T_{R1}, T_{R2}, and T_M) from $\rho(T)$, $S(T)$, and $\kappa(T)$ data, RRR at 300 K, Fermi energy (E_F) in $B2$-phase, ratio of electronic to lattice thermal conductivity (κ_e/κ_L) at 300 K, and entropy change (ΔS) at T_{R2} for aged $Ti_{50-x}Ni_{48+x}Fe_2$ ($x = 0.0 - 2.0$) alloys.

Aged alloys	MT temperatures (K) from $\rho(T)$			RRR	MT temperatures (K) from $S(T)$			E_F (eV)	MT temperatures (K) from $\kappa(T)$			κ_e/κ_L ratio	ΔS (J/mol K) at T_{R2}
	T_{R2}	T_{R1}	T_M		T_{R2}	T_{R1}	T_M		T_{R2}	T_{R1}	T_M		
0.0		264.4	212.1	1.41		265.2	221.3	2.1		265.6	223.2	4.3	
0.5	260.0	228.0	174.5	1.10	262.0	228.8	176.1	2.3	259.2	227.0	173.6	1.2	
1.0	257.5			1.28	255.9			2.1	256.0			0.9	2.25
1.5	251.3			1.16	249.8			2.0	251.8			5.2	1.85
2.0	248.8			1.23	245.7			1.9	249.1			1.3	1.40

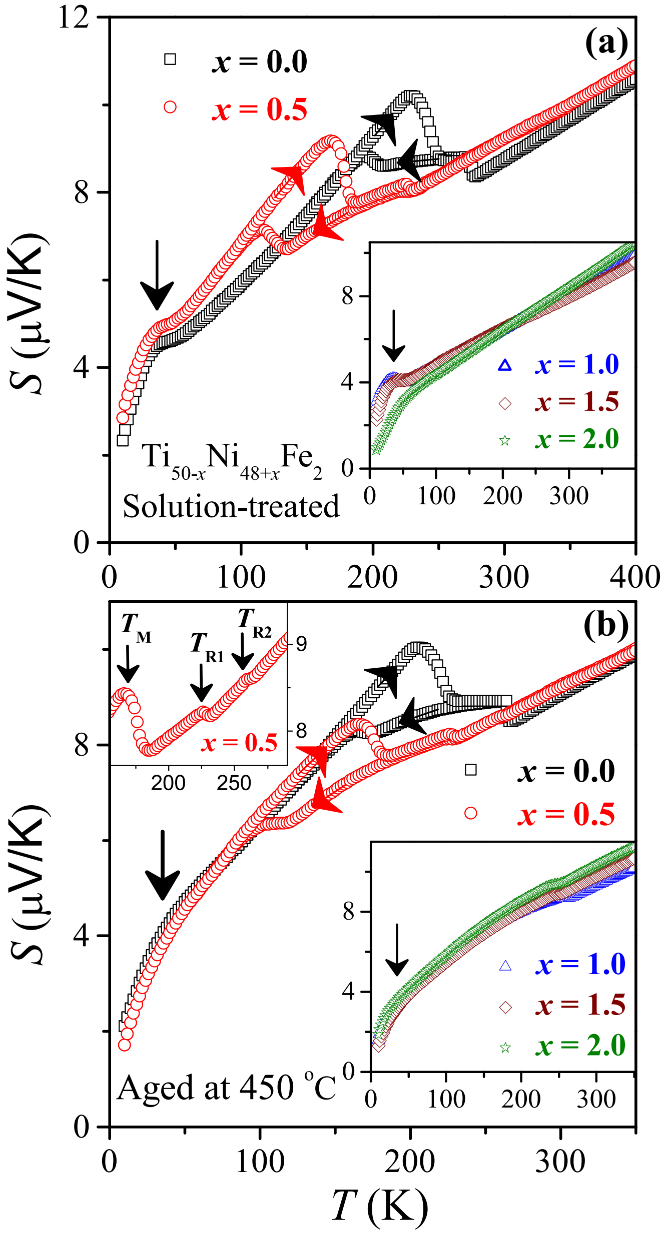

FIG. 2. (a) Temperature-dependent Seebeck coefficient $S(T)$ of solution-treated $Ti_{50-x}Ni_{48+x}Fe_2$ SMAs with $x = 0.0$ and 0.5 during cooling and warming cycles. Inset shows $S(T)$ data for $x = 1.0$, 1.5, and 2.0 compositions. (b) $S(T)$ for thermally aged alloys with $x = 0.0$ and 0.5. Lower inset shows $S(T)$ data for $x = 1.0$, 1.5, and 2.0 compositions. Upper inset highlights characteristics at T_{R1}, T_{R2}, and T_M transitions during warming cycle for $x = 0.5$ sample. Phonon-drag features at low temperatures are indicated by vertical arrows.

values at T_{R2} for these samples is comparable to that at T_{R1}; however, it is much smaller than that at T_M. It suggests that the modulation of the electronic band structure or the change in the DOS at the Fermi level for T_{R1} and T_{R2} are the same.

Below the MT temperatures, the $S(T)$ curves of the two sets of alloys change almost linearly with temperatures until 50 K, indicating a typical metallic diffusive behavior. A humplike feature for temperatures below 50 K in all studied alloys was visible (indicated by arrows in Fig. 2), resulting from the phonon-drag effect [16,17,27]. The phonon-drag effect is commonly seen in high-quality crystalline solids at low temperatures. Figure 2(b) shows a suppression of the hump in the aged $Ti_{50-x}Ni_{48+x}Fe_2$ samples, presumably attributed to the formation of the Ti_3Ni_4 precipitates that gives rise to more impurities and structural disorders in the system. In metals with dominant single-band transport, the S is expected to have a linear function with temperature and can be expressed by Mott's formula, $S = \pi^2 k_B^2 T/2eE_F$, where k_B is the Boltzmann constant, e is the electron charge, and E_F is the Fermi energy. The E_F values of all these samples were obtained by linear fitting the $S(T)$ data in the high-temperature austenite $B2$ phase using Mott's equation and are listed in Tables I and II. The E_F values for these two series of alloys varied between 1.8 and 2.3 eV, which agrees with the metallic nature of other TiNi-based alloys [15–18]. Such a finding indicates that the DOS near the E_F or electronic structure of these alloys in the high-temperature $B2$ phase are almost comparable, although they have different MT characteristics at low temperatures. We also found that the S values of these alloys in the parent $B2$ phase lie between 9 and 11 μV/K, indicating that the charge-carrier scattering and the mobility of charge carriers for the thermoelectric transport had no significant variation with Ti/Ni ratio and the formation of precipitates in the $Ti_{50-x}Ni_{48+x}Fe_2$ SMAs.

C. Specific heat

To study the thermal properties of both series of $Ti_{50-x}Ni_{48+x}Fe_2$ ($x = 0.0-2.0$) SMAs, the temperature variation of specific heat $C_P(T)$ was measured during the warming cycle. The $C_P(T)$ data of solution-treated samples with $x = 0.0$ and 0.5, shown in Fig. 3(a), display a sharp peaklike feature near 290 K due to the $R1$-phase transformation and no discernible peak anomaly due to the $B19'$-phase transformation [13,17,50]. The peak height for $R1$-phase transformation (∼230 K) in the $x = 0.5$ sample was lower than in the $x = 0.0$ sample, implying a weaker $R1$-transformation strain (or transformation heat), consistent with the electrical transport property measurements [17,22,50]. The $B19'$-phase transformation in $C_p(T)$ for these samples was not detected, probably because of its large transformation hysteresis and transformation width, similar to other Fe-doped and Ni-rich TiNi-based alloys [13,17,50]. On the other hand, the $C_P(T)$ of $x = 1.0$, 1.5, and 2.0 samples showed no detectable anomalous features associated with the STG transition over the entire temperatures of our investigation [13,16,17,22,27].

The $C_p(T)$ data for the 450 °C aged $Ti_{50-x}Ni_{48+x}Fe_2$ samples shown in Fig. 3(b) display a similar sharp peaklike shape at $T_{R1} \simeq 265$ K for the $x = 0.0$ sample. The $Ti_{50}Ni_{48}Fe_2$ sample also shows a broad humplike feature near 222 K for the $B19'$-phase transition. For the $x = 0.5$ sample, $C_p(T)$ displayed two distinct peak anomalies around 232 and 259 K corresponding to the $R1$- and $R2$-phase transformations, respectively, but no detectable peak anomaly due to the $B19'$-phase transformation. In contrast, the $x = 1.0$, 1.5, and 2.0 alloys showed only a peak in $C_p(T)$ near 257, 253, and 248 K, respectively, due to the transformation of the $R2$ phase. It is noted that the shape and size of the $C_p(T)$ peak for the T_{R2} in $Ti_{50-x}Ni_{48+x}Fe_2$ SMAs is composition dependent. In

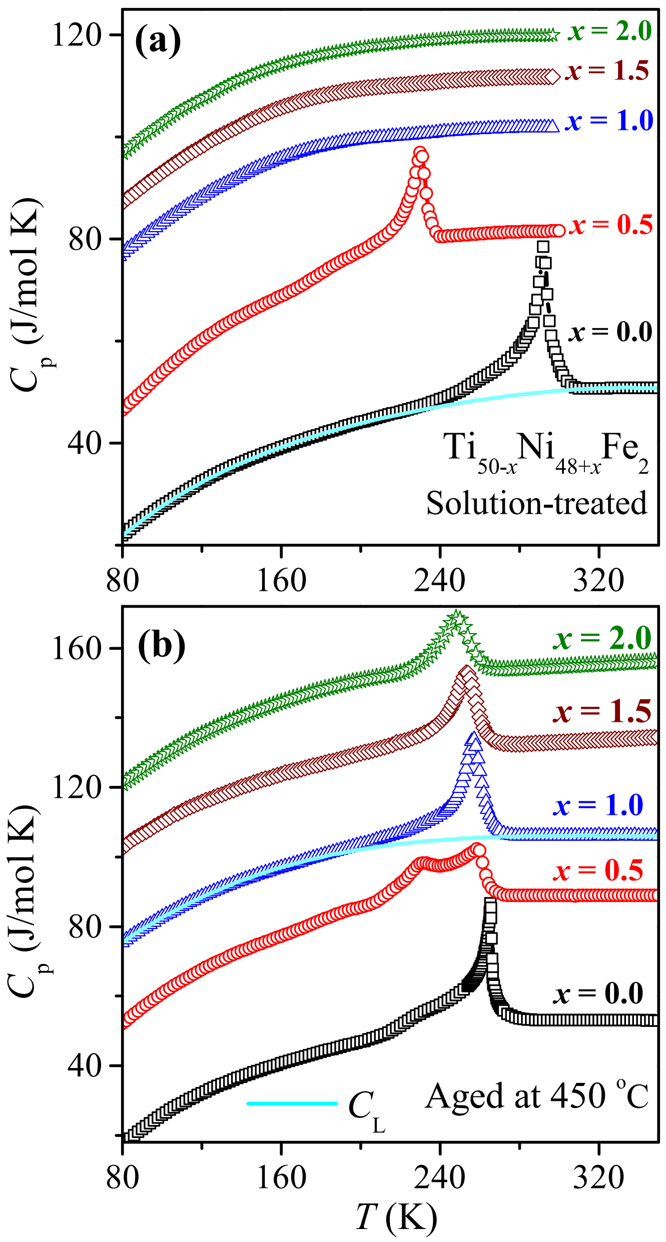

FIG. 3. Temperature variation of specific heat $C_p(T)$ of (a) solution-treated and (b) 450 °C aged Ti$_{50-x}$Ni$_{48+x}$Fe$_2$ SMAs with $x = 0.0$, 0.5, 1.0, 1.5, and 2.0 during warming cycle. Solid lines represent lattice-specific heat contribution (C_L) by a polynomial fit of $C_p(T)$ far from transition. All $C_p(T)$ curves have been offset vertically for clarity.

particular, the $C_p(T)$ peak at T_{R2} was highest in the $x = 1.0$ sample and decreased gradually with increasing x values. Such findings agree with the previous study of variations in precipitate size and the enthalpy change across T_{R2} (using DSC measurements) with x, implying that the $x = 1.0$ sample contains a larger volume of $R2$ phases within the $B2$ matrix than the other samples [46,47].

As can be seen from Figs. 3(a) and 3(b), the $C_p(T)$ of both series of alloys show a tendency for saturation at high temperatures. The room temperature C_p value lies between 50 and 55 J/mol K. These values are very close to the expected Dulong-Petit value $C_V = 3mR = 6R = 49.8$ J/mol K, where R is the ideal-gas constant, and m is the number of atoms per formula unit. To calculate the change in entropy (ΔS) across the MTs, a smooth lattice background contribution (C_L) was generated by fitting the $C_p(T)$ data far from the transition region and is illustrated by solid lines in Fig. 3. Here, the entropy change associated with two-stage R-phase transformations (i.e., $R1$ and $R2$) in the $x = 0.5$ aged sample was difficult to estimate because these transitions were very close to one another and the background was hard to define. The ΔS at $R1$- and $R2$-phase transitions for other samples were estimated by subtracting the C_L and are listed in Tables I and II. These show that ΔS for the $R1$ and $R2$-phase transitions of the two series of alloys decreased with increasing x.

D. Thermal conductivity

The temperature variation of thermal conductivity $\kappa(T)$ during the warming cycle for both series of Ti$_{50-x}$Ni$_{48+x}$Fe$_2$ ($x = 0.0 - 2.0$) SMAs is shown in Fig. 4. The $\kappa(T)$ of the solution-treated samples with $x = 0.0$ and 0.5 exhibited two steplike jumps near the $B19' \rightarrow R1$ and $R1 \rightarrow B2$ MTs, as shown in Fig. 4(a). The steplike jump at T_{R1} and T_M differed from a spike-shaped anomaly in the Ti$_{50}$Ni$_{50-x}$Fe$_x$ SMAs with $x \leqslant 2.0$ but was similar to the samples with $x \geqslant 2.0$ [17,50]. It indicates that the electron-phonon coupling near the MTs was weak in Ti$_{50}$Ni$_{48}$Fe$_2$ SMA. Further weakening of electron-phonon coupling in the Ni-rich Ti$_{50-x}$Ni$_{48+x}$Fe$_2$ alloys was seen as the jump in κ associated with the MTs decreased with increasing x [17,44]. The samples with $x = 1.0$–2.0 exhibited no anomalies in $\kappa(T)$ for the STG transition [see Fig. 4(b)], similar to that observed in the Ti$_{50}$Ni$_{50-x}$Fe$_x$ SMAs for $x \geqslant 6.0$ and Ni-rich Ti$_{50-x}$Ni$_{50+x}$ SMAs for $x \geqslant 1.3$ [16,17,27], as a result of complete suppression of the electron-phonon coupling [44]. The MT temperatures obtained from $\kappa(T)$ are presented in Table I and are consistent with the $\rho(T)$ and $S(T)$ measurements. Furthermore, at low temperatures, $\kappa(T)$ for the $x = 0.0$ and 0.5 samples increased rapidly with temperatures until 50 K, attributed to the contribution of thermally excited phonons. On the other hand, $\kappa(T)$ for the $x = 1.0 - 2.0$ samples increased linearly with temperatures, inferring the absence of soft phonon modes in the STG phase [17,53].

Figure 4(c) shows the $\kappa(T)$ of the 450 °C aged Ti$_{50}$Ni$_{48-x}$Fe$_2$ SMAs with $x = 0.0$ and 0.5. We found a steplike jump accompanied by a pronounced spike-shaped peak with $\Delta\kappa/\kappa \sim 28\%$ across the $R1$-phase transformation, while a steplike jump at the $B19'$-phase transformation for the $x = 0.0$ sample. The spike-shaped anomaly for the $R1$-phase transformation is unusual and will be discussed in the next paragraph. On the other hand, the $x = 0.5$ sample did not show spikelike peak anomalies and exhibited a steplike jump at the T_{R1} and T_M. Besides, a slight slope change near 259 K indicated the existence of the $R2$-phase transformation in this alloy [see inset of Fig. 4(c)]. In contrast, $\kappa(T)$ of the $x =$ 1.0–2.0 samples showed a prominent steplike jump at T_{R2} [see Fig. 4(d)], consistent with the $S(T)$ results. In Table II, we found a good agreement between the MT temperatures obtained from $\kappa(T)$ and those obtained from other transport measurements. Figure 4(d) illustrates that the intermediate $R2$ phase exhibits lower κ values than the high-temperature $B2$ phase, which can be explained by the lower hardness of

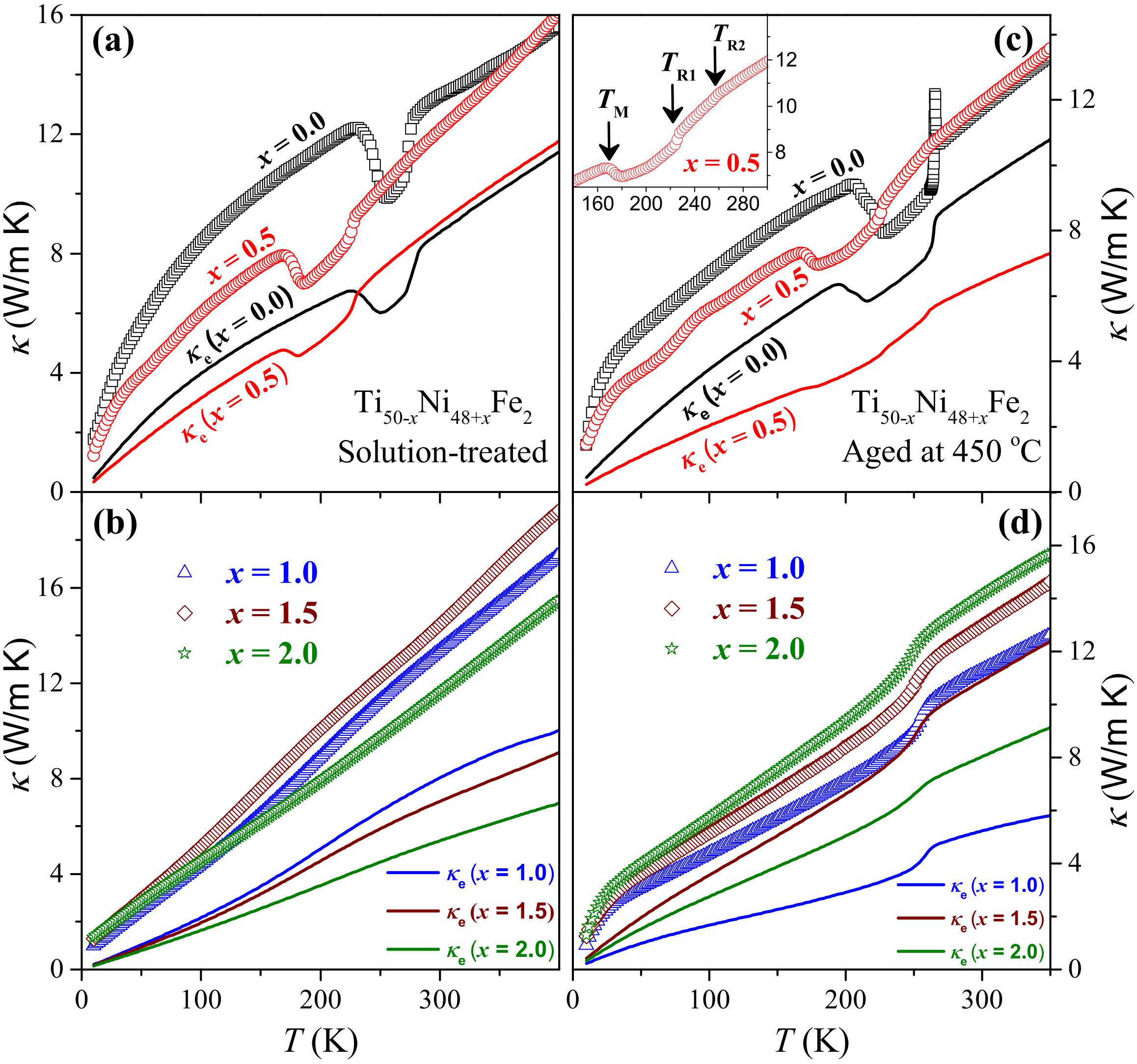

FIG. 4. Temperature-dependent thermal conductivity $\kappa\ (T)$ of solution-treated $Ti_{50-x}Ni_{48+x}Fe_2$ SMAs with (a) $x = 0.0$ and 0.5 and (b) $x = 1.0$, 1.5, and 2.0. $\kappa\ (T)$ for thermally aged alloys with (c) $x = 0.0$ and 0.5 and (d) $x = 1.0$, 1.5, and 2.0. Inset in (c) highlights characteristics near T_{R1}, T_{R2}, and T_M transitions for $x = 0.5$ sample. Solid lines represent electronic contribution of thermal conductivity $\kappa_e(T)$ for these alloys estimated using Weidemann-Franz law.

the *R* phase than the *B*2 phase [54]. It also suggests that the hardening of phonon modes in the *B*2 phase, which results from Ti_3Ni_4 precipitates, is similar to that observed in the aged $Ti_{48.7}Ni_{51.3}$ alloy [36].

The room-temperature κ values of all studied samples lay between 10.0 and 15.0 W/m K, comparable with the κ values of the previous report of Fe-doped TiNi SMAs [17,50]. However, these values were slightly lower than that of the equiatomic $Ti_{50}Ni_{50}$ SMA (∼17 W/m K) [16,50]. The $\kappa(T)$ measurements can provide valuable information about different thermal scattering processes such as charge and phonon carriers; therefore, it is essential to investigate the role of charge and phonon carriers in the heat conduction of present SMAs. In general, the total κ of metal can be expressed as a sum of electronic (κ_e) and lattice (κ_L) terms, i.e., $\kappa = \kappa_e + \kappa_L$. The κ_e contribution could be obtained by using the Wiedemann-Franz law, $\kappa_e = L_0T/\rho$, where ρ is the electrical resistivity and L_0 ($= 2.45 \times 10^{-8}\ \mathrm{W\Omega/K^2}$) is the Lorentz number and is shown in Fig. 4 by the solid lines. The κ_L contribution of these alloys was then calculated by subtracting the κ_e from the measured κ. From this estimation, it was noted that the κ_e/κ_L ratio was larger than the one in the *B*2 phase for both series of samples (see Tables I and II), similar to the observation in Cu- and Ni-doped TiNi SMAs [15,16,50].

The variation of $\kappa_e(T)$ of the studied $Ti_{50-x}Ni_{48-x}Fe_2$ SMAs roughly followed the same trend as the total $\kappa(T)$. A pronounced jump in κ_e near the T_{R2}, T_{R1}, and T_M corresponded to the observed steplike feature in the $\rho(T)$ (see Fig. 1). The $\kappa_L(T)$ also showed steplike jumps near the MT temperature regions (not shown here); however, their magnitudes were small than those in $\kappa_e(T)$. Besides, we observed that $\kappa_L(T)$ does not follow the $C_p(T)$ behavior [see Figs. 3(a) and 3(b)], especially the peak-shaped anomaly across the MTs for these samples, i.e., $\kappa_L(T)$ does not obey the classical kinetic theory of lattice thermal conductivity ($\kappa_L \propto C_p$) near the MT regions [36,50]. It implies that the *R*1, *R*2, and *B*19′-phase transitions in the $Ti_{50-x}Ni_{48+x}Fe_2$ SMAs are essentially associated with electronic contributions. However, the spike-shaped anomaly in $\kappa(T)$ near T_{R1} for the $x = 0.0$ aged sample was ascribed to the phonon contribution. There was extra scattering with heat-carrying soft phonons, similar to the observations in our previous work on the $R1$-phase transformation of solution-treated $Ti_{50}Ni_{48.5}Fe_{1.5}$ SMA [50]. In contrast, in the samples with STG behavior for $x = 1.0–2.0$ (solution treated), neither $\kappa_e(T)$ nor $\kappa_L(T)$ showed any noticeable anomalies in the temperature range under investigation. The suppression of anomalous features was presumably attributed to excess Ni atoms occupying the Ti vacancy as antisite defects [16,17,27].

IV. DISCUSSION

The above results confirm that the point defects introduced by an excess of Ni and the formation of Ti_3Ni_4 precipitates with thermal aging in the $Ti_{50-x}Ni_{48+x}Fe_2$ SMAs showed distinct anomalies in the measured physical properties near the MT characteristic temperatures. We found that both point defects and precipitates can produce random strain fields in $Ti_{50-x}Ni_{48+x}Fe_2$ alloys and overcome the local energy barriers to stabilize the low-strain R phase [4,17,22,36]. However, a competition between the thermodynamic driving force and the kinetic slowdown for the R-phase formation due to the local frustration of these defects was in the TiNi lattice. Based on our findings, a quantitative T vs x phase diagram for two series of $Ti_{50-x}Ni_{48+x}Fe_2$ alloys was proposed in Figs. 5(a) and 5(b). In the phase diagram, the characteristic temperatures of T_{R1}, T_{R2}, and T_M were taken from the high-precision $S(T)$ measurement, whereas the temperature of T_G was taken from the $\rho(T)$ measurement during the warming cycle. Despite their composition and synthesis processes, both sets of alloys appeared to remain in the parent $B2$ phase at high temperatures; however, at low temperatures, they underwent different phase transformations.

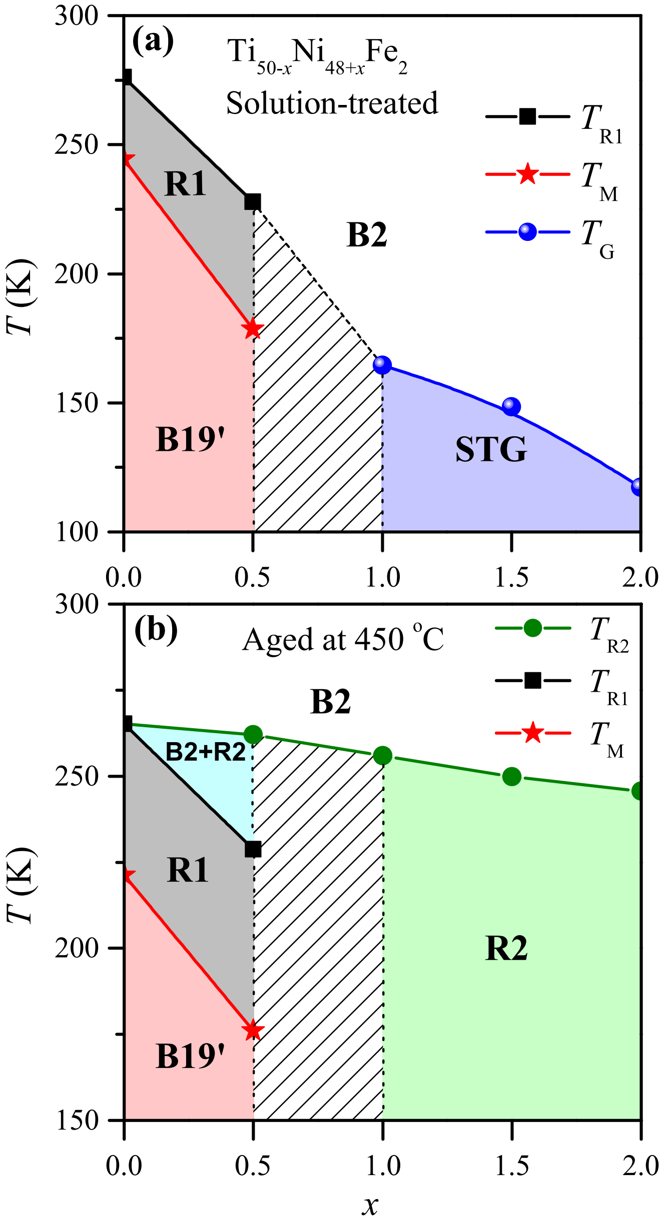

FIG. 5. T vs x phase diagram of (a) solution-treated and (b) 450 °C aged $Ti_{50-x}Ni_{48+x}Fe_2$ alloys, derived from electrical transport measurements, represents parent $B2$ austenite, $R1$ and $R2$ premartensite, $B19'$ martensite, and STG phase regions. Solid lines are a guide to the eye. Critical concentration of Ni (x_c) at which STG phase (T_G) in solution-treated samples and intermediate $R2$-phase transformation (T_{R2}) in aged samples must lie within range of $0.5 < x < 1.0$, as indicated by hatched fillings.

The solution-treated $Ti_{50}Ni_{48}Fe_2$ alloy exhibited two-step MTs, i.e., $B2 \leftrightarrow R1$ (T_{R1}) and $R1 \leftrightarrow B19'$ (T_M) below 300 K. Increasing point defects with an excess of Ni in $Ti_{50-x}Ni_{48+x}Fe_2$ alloys lowered the T_{R1} and T_M values [see Fig. 5(a)], as more local strain fields were developed in the $B2$ matrix [16,17,22,30]. The T_{R1} and T_M transitions disappeared for $x \geqslant 1.0\%$ of Ni excess, and the system showed the STG behavior at low temperatures. It is worth mentioning that the crossover from martensite to STG phase in $Ti_{50}Ni_{50-x}Fe_x$ and $Ti_{50-x}Ni_{50+x}$ SMAs was previously reported for a critical Fe and Ni concentration of $x \approx 6.0$ and 1.3, respectively [12,17,27,28]. In this study, the critical concentration of Ni (x_C) at which the STG phase appears in $Ti_{50-x}Ni_{48+x}Fe_2$ alloys has not been precisely optimized. However, it must lie in the range of $0.5 < x < 1.0$, as indicated by the hatched fillings in Fig. 5(a). The T_G transition for $x \geqslant 1.0\%$ Ni is mainly attributed to the dominance of the kinetic local barrier process (i.e., defects) over the thermodynamic driving force (i.e., thermal activation energy k_BT), thereby significantly reducing the thermodynamic stability of the martensite phase in $Ti_{50-x}Ni_{48+x}Fe_2$ alloys. Interestingly, the appearance of the STG phase in $Ti_{50-x}Ni_{48+x}Fe_2$ alloys was found to be strongly compositional dependent, i.e., it occurred only for 3% of the total amount of Ni and Fe, while it has been observed in Fe-doped TiNi alloys for $x \geqslant 6\%$ [13,17]. Ramachandran *et al.* also observed an occurrence of the STG phase from the R phase in $Ti_{50}Ni_{44}Fe_6$ SMA with a small addition of Ni (∼1%), suggesting that the length scale of atomic-scale strain randomness is considerably larger when the Ni/Ti ratio increases in comparison to the point defects with Fe substitutions [17,55].

In contrast, the Ti_3Ni_4 precipitates in the aged $Ti_{50-x}Ni_{48+x}Fe_2$ alloys generate additional strain fields in the $B2$ matrix and alter the MT characteristics. Previously, microstructural studies in Ni-rich aged alloys at 450 °C for 100 h with the same composition showed that Ti_3Ni_4 precipitates grew in large quantities in the $B2$ matrix because the total Ni and Fe contents were greater than Ti [46,47]. The $Ti_{50}Ni_{48}Fe_2$ alloy showed only T_{R1} and T_M transitions [see Fig. 5(b)], similar to that of the solution treated, as no precipitates were detected in the $B2$ phase. However, the alloy with $x = 0.5$ led to the occurrence of another R phase transition due to precipitates [46,47]. This is primarily attributed to the generation of local lattice deformations ascribed by the coherent interface between precipitates and the $B2$ matrix [4,36]. The two-stage R transformation in $x = 0.5$ was most likely due to the competition between point defects and precipitates rather than inhomogeneous precipitation between grain boundaries and grain interiors, as both regions have relatively homogeneous distributions of precipitates [46,47]. Also, the parent $B2$ phase and intermediate $R2$ phase will likely coexist within the range of $T_{R1} < T < T_{R2}$. For $x \geqslant 1.0$, T vs x diagram of the aged $Ti_{50-x}Ni_{48+x}Fe_2$ alloys only showed the T_{R2} transition. We could not precisely identify the critical composition of Ni (x_C) where T_{R1} disappears, and T_{R2} remains in the aged $Ti_{50-x}Ni_{48+x}Fe_2$ alloys. It is well known that when the precipitate sizes in the $B2$ matrix are large and their distribution is homogeneous, the strain randomness is lower, and only T_{R2} transition occurs [4,36]. In this case, x_C should lie in the $0.5 < x < 1.0$ range, as indicated by hatched fillings in Fig. 5(b). For $x > 1.0$, T_{R2} decreases, mainly due to the competition between internal strain/stress and changes in the chemical composition of the $Ti_{50-x}Ni_{48+x}Fe_2$ matrix caused by precipitations.

Furthermore, we noticed that the T_{R2} in the aged alloy with $x = 0.5$ occurred at higher temperatures than the T_{R1} [see Fig. 5(b)]. A similar trend was reported for the precipitate-induced STG phase, in which the T_G was higher (>200 K) than that of the point defect-induced T_G (<175 K) [39,43]. This further suggests that the length scale of strain-field randomness due to point defects is larger than that in the precipitates in the aged $Ti_{50-x}Ni_{48+x}Fe_2$ SMAs [4,40]. Besides, the T_{R1} values in the Ni-rich aged samples are slightly different from those in the solution-treated samples (see Fig. 5), presumably due to a competition between the increasing Fe and decreasing Ni contents in the matrix, as Ti_3Ni_4 precipitates reduce the Ni content but increase the Fe content. In addition, Ti_3Ni_4 precipitates may also pose a strong resistance to the lattice strain associated with $B19'$ transformation. Thus, T_M values were lower than those obtained from the solution-treated samples. Ultimately, T_{R1} and T_M have suppressed for $x \geqslant 1.0$ aged samples, where the size (or domain) of precipitates was reported to be extremely large (>100 nm) [46,47].

Other important results in the present study include the negative TCR (or semiconducting-like) behavior at low temperatures below T_G in the solution-treated alloys with $x = 1.0-2.0$, whereas aged alloys with similar compositions display a normal metal-like behavior at low temperatures below T_{R2} [see Fig. 1]. This provides an insight into the origin of the negative TCR behavior observed in non-martensitic transitions of Fe-doped TiNi alloys [13,17,28,29]. Fe-doped TiNi alloys form the local strain ordering of R domains prior to the MT, which has higher ρ values than the parent $B2$ phase. In the $Ti_{50-x}Ni_{48+x}Fe_2$ alloys, R-like domains are also formed in the $B2$ phase as the temperature decreases. In the solution-treated alloys, however, when $x \geqslant 1.0$, R domains start freezing below T_G due to excessive atomic-scale point defects. Thus, negative TCR below T_G is caused by the continuous formation and growth of R domains in these alloys. In contrast, most of the excess Ni precipitates as Ti_3Ni_4 in the Ni-rich aged alloys. As we previously discussed, aged alloys for $x \geqslant 1.0$ showed less strain randomness due to the larger precipitate size; thus, the alloys displayed long-range strain-ordering R-phase transition with decreasing temperature, resulting in metal-like behavior in $\rho(T)$ at low temperatures.

We employed the ferroelastic models to explain the observed decrease in entropy change (ΔS) associated with the R-phase transformation with x in two series of $Ti_{50-x}Ni_{48+x}Fe_2$ alloys [see Tables I and II]. According to the Landau free-energy model [56], $\Delta S = -Ae_M^2$, where A is a proportionality constant, and e_M is the lattice distortion (or transformation strain) at the MT temperatures. The minus sign indicates that MT always results in a decrease in entropy. The above relation suggests that the larger the transformation strain, the larger the value of ΔS. Therefore, our observed decrease in ΔS values with increasing x for both T_{R1} and T_{R2} transitions suggests that the transformation heat ($\propto \Delta S$) decreased with decreasing the transformation strain [13,17,56]. These observations are analogous to those studies in the Ni-rich $Ti_{48.7}Ni_{51.3}$ aged alloys and $Ti_{50}Ni_{50-x}Fe_x$ solution-treated alloys [17,36]. Moreover, the magnitudes of ΔS for two R-phase transformations in $Ti_{50-x}Ni_{48+x}Fe_2$ samples were considerably lower than those for $B2 \leftrightarrow B19$ and $B2 \leftrightarrow B19'$ transformations in TiNi-based SMAs, (i.e., $|\Delta S|_R < |\Delta S|_{B19} < |\Delta S|_{B19'}$), indicating that the intermediate R phase produced by either point defects or precipitates had a smaller transformation strain (or ΔS) than the $B19'$ phase transformation [4,15,17,36,50].

V. CONCLUSION

In summary, we systematically investigated the temperature-dependent electrical and thermal properties of two series of $Ti_{50-x}Ni_{48+x}Fe_2$ ($x = 0.0-2.0$) SMAs after solution treated and thermally aged at 450 °C via electrical resistivity, Seebeck coefficient, specific heat, and thermal conductivity measurements. The point defects induced by increasing Ni/Ti ratios and the formation of Ti_3Ni_4 precipitates with thermal aging in $Ti_{50-x}Ni_{48+x}Fe_2$ SMAs significantly altered the MT characteristics and exhibited distinct properties in all measured physical quantities. The MT characteristics of the $Ti_{50}Ni_{48}Fe_2$ sample in both series of alloys showed two-step $B2 \leftrightarrow R1 \leftrightarrow B19'$ MT. With increasing Ni/Ti ratios, the MT characteristics in solution-treated alloys with $x \geqslant 1.0$ destroyed the T_{R1} and T_M ordering and formed the STG phase. In contrast, the aged alloys showed another $R2$-phase transition due to the presence of Ti_3Ni_4 precipitates at higher temperatures than the T_{R1} and T_M in Ni-rich $Ti_{50-x}Ni_{48+x}Fe_2$ SMAs. When $x \geqslant 1.0$, only T_{R2} survived while T_{R1} and T_M were suppressed, and no STG ordering was observed.

The electrical properties using $\rho(T)$ and $S(T)$ revealed the metallic nature in two sets of $Ti_{50-x}Ni_{48+x}Fe_2$ alloys, while RRR, TCR, and phonon-drag features vary significantly with increasing Ni/Ti ratios. These observations indicate that chemical disorders, point defects, and impurities (or precipitates) significantly affect the electrical properties in the Ni-rich $Ti_{50-x}Ni_{48+x}Fe_2$ SMAs. Besides this, the solution-treated alloys with $x \geqslant 1.0$ exhibit a negative TCR at low temperatures in the STG phase due to the continuous formation and growth of R domains. In the $S(T)$ measurements, the scattering of charge carriers (mostly holes) in both series of $Ti_{50-x}Ni_{48+x}Fe_2$ alloys appears to be composition independent at $B2$ phase, and the electronic band structure or the DOS near the Fermi level varies substantially at the MTs. Further analysis of the $\kappa(T)$ data revealed that the electronic contribution to all MT characteristics is greater than the contribution of phonons. As Ni content increases, the electron-phonon coupling weakens, and phonon modes become harder in both series of alloys. For two series of $Ti_{50-x}Ni_{48+x}Fe_2$ alloys, the entropy changes across the T_{R1} and T_{R2} transformations are estimated by $C_p(T)$, which decrease with the lowering of the MT temperatures (or the transformation strains). This can be explained in the framework of the Landau free-energy model. The phase diagrams are constructed for both series of alloys, indicating that the critical composition responsible for the STG phase in solution-treated alloys and the R-phase transition in aged alloys must lie in the range of $0.5 < x < 1.0$ for the $Ti_{50-x}Ni_{48+x}Fe_2$ alloys.

ACKNOWLEDGMENTS

This work was supported by the National Science and Technology Council of Taiwan under Grants No. NSTC 112-2112-M-259-012 (YKK) and No. NSTC 109-2221-E-002-120-MY2 (SKW).

---

[1] K. Shimizu and T. Tadaki, *Shape Memory Effect: Mechanism in Shape Memory Alloys* (Gordon and Breach Science, New York, 1987).

[2] K. Otsuka and C. M. Wayman, *Shape Memory Materials* (Cambridge University Press, Cambridge, England, 1998).

[3] C. M. Wayman, Shape memory alloys, MRS Bull. **18**, 49 (1993).

[4] K. Otsuka and X. Ren, Physical metallurgy of TiNi-based shape memory alloys, Prog. Mater. Sci. **50**, 511 (2005).

[5] P. K. Kumar and D. C. Lagoudas, *Introduction to Shape Memory Alloys* (Springer, Boston, 2008).

[6] M. López-Medina, F. Hernández-Navarro, H. Flores-Zúñiga, and D. E. Soto-Parra, Reversible elastocaloric effect related to B2-R transformation in $Ni_{50.5}Ti_{49.5}$ alloy, J. Appl. Phys. **129**, 115104 (2021).

[7] J. Van Humbeeck, Shape memory alloys: A material and a technology, Adv. Eng. Mater. **3**, 837 (2001).

[8] S. K. Wu and H. C. Lin, Recent development of TiNi-based shape memory alloys in Taiwan, Mater. Chem. Phys. **64**, 81 (2000).

[9] J. Y. Lee, G. C. Mclntosh, A. B. Kaiser, Y. W. Park, M. Kaack, J. Pelzl, C. K. kim, and K. Nahm, Thermopower behavior of shape memory alloy NiTi, J. Appl. Phys. **89**, 6223 (2001).

[10] V. Wadhawan, *Introduction to Ferroic Materials* (CRC Press, Boca Raton, FL, 2000).

[11] J. A. Mydosh, *Spin Glasses: An Experimental Introduction* (Taylor & Francis, London, 1993).

[12] Z. Zhang, Y. Wang, D. Wang, Y. Zhou, K. Otsuka, and X. Ren, Phase diagram of $Ti_{50-x}Ni_{50+x}$: Crossover from martensite to strain glass, Phys. Rev. B **81**, 224102 (2010).

[13] M. S. Choi, T. Fukuda, and T. Kakeshita, Anomalies in resistivity, magnetic susceptibility and specific heat in iron doped Ti-Ni based shape memory alloys, Scr. Mater. **53**, 869 (2005).

[14] Y. Zhou, D. Xue, X. Ding, Y. Wang, J. Zhang, Z. Zhang, D. Wang, K. Otsuka, J. Sun, and X. Ren, Strain glass in doped $Ti_{50}(Ni_{50-x}D_x)$ (D = Co, Cr, Mn) alloys: Implication for the generality of strain glass in defect-containing ferroelastic systems, Acta Mater. **58**, 5433 (2010).

[15] B. Ramachandran, R. C. Tang, P. C. Chang, Y. K. Kuo, C. Chien, and S. K. Wu, Cu-substitution effect on the thermoelectric properties of the TiNi-based shape memory alloys, J. Appl. Phys. **113**, 203702 (2013).

[16] B. Ramachandran, C. H. Chen, P. C. Chang, Y. K. Kuo, C. Chien, and S. K. Wu, Thermal and transport properties of as-grown Ni-rich TiNi shape memory alloys, Intermetallics **60**, 79 (2015).

[17] B. Ramachandran, P. C. Chang, Y. K. Kuo, C. Chien, and S. K. Wu, Characteristics of martensitic and strain-glass transitions of the Fe-substituted TiNi shape memory alloys probed by transport and thermal measurements, Sci. Rep. **7**, 16336 (2017).

[18] G.-L. Zhao, T. C. Leung, B. N. Harmon, M. Keil, M. Mullner, and W. Weber, Electronic origin of the intermediate phase of NiTi, Phys. Rev. B **40**, 7999 (1989).

[19] S. M. Shapiro, J. Z. Larese, Y. Noda, S. C. Moss, and L. E. Tanner, Neutron-scattering Study of Premartensitic Behavior in Ni-Al Alloys, Phys. Rev. Lett. **57**, 3199 (1986).

[20] J. M. Zhang and G. Y. Guo, Electronic structure and phase stability of three series of B2 Ti-transition-metal compounds, J. Phys. Condens. Matter **7**, 6001 (1995).

[21] T. Yamamoto, T. Fukuda, and T. Kakeshita, Electronic structure of B2-type Ti-Ni-Fe alloys exhibiting second-order-like structural transformation, Mater. Trans. **47**, 594 (2006).

[22] J. Frenzel, A. Wieczorek, I. Opahle, B. Maaß, R. Drautz, and G. Eggeler, On the effect of alloy composition on martensitic start temperatures and latent heat in Ni-Ti-based shape memory alloys, Acta Mater. **90**, 213 (2015).

[23] Y. Wang, X. Ren, and K. Otsuka, Shape Memory Effect and Superelasticity in a Strain Glass Alloys, Phys. Rev. Lett. **97**, 225703 (2006).

[24] S. Sarkar, X. Ren, and K. Otsuka, Evidence of Strain Glass in the Ferroelastic-Martensitic System $Ti_{50-x}Ni_{50+x}$, Phys. Rev. Lett. **95**, 205702 (2005).

[25] Y. Ji, D. Wang, X. Ding, K. Otsuka, and X. Ren, Origin of an Isothermal R-Martensite Formation in Ni-rich Ti-Ni Solid Solution: Crystallization of Strain Glass, Phys. Rev. Lett. **114**, 055701 (2015).

[26] Q. Liang, D. Wang, J. Zhang, Y. Ji, X. Ding, Y. Wang, X. Ren, and Y. Wang, Novel B19′ strain glass with large recoverable strain, Phys. Rev. Mater. **1**, 033608 (2017).

[27] P. Bag, P. C. Chang, Y. K. Kuo, S. K. Wu, C. Lin, and B. Y. Li, Coexistence of martensite and strain glass phases in homogenized Ni-rich TiNi shape memory alloys, Intermetallics **109**, 16 (2019).

[28] S. Hou, Y. Wang, J. Zhang, D. Wang, S. Ren, and X. Ren, Evidence for crossover martensite in $Ti_{50}Ni_{45}Fe_5$: An intermediate state between normal martensite and strain glass, Euro. Phys. Lett. **100**, 58001 (2012).

[29] D. Wang, Z. Zhang, J. Zhang, Y. Zhou, Y. Wang, X. Ding, Y. Wang, and X. Ren, Strain glass in Fe-doped Ti-Ni, Acta Mater. **58**, 6206 (2010).

[30] D. Wang, Y. Wang, Z. Zhang, and X. Ren, Modeling Abnormal Strain States in Ferroelastic Systems: The Role of Point Defects, Phys. Rev. Lett. **105**, 205702 (2010).

[31] X. Ren, Y. Wang, Y. Zhou, Z. Zhang, D. Wang, G. Fan, K. Otsuka, T. Suzuki, Y. Ji, and J. Zhang *et. al.*, Strain glass in ferroelastic systems: Premartensitic tweed versus strain glass, Philos. Mag. **90**, 141 (2010).

[32] R. Nevgi, S. Pollastri, G. Aquilanti, and K. R. Priolkar, Structural defects responsible for the strain glassy transition in $Ni_{50+x}Ti_{50-x}$, Phys. Rev. B **103**, 064108 (2021).

[33] S. Miyazaki, Y. Igo, and K. Otsuka, Effect of thermal cycling on the transformation temperatures of TiNi alloys, Acta Metall. **34**, 2045 (1986).

[34] M. Nishida, T. Hara, T. Ohba, K. Yamaguchi, K. Tanaka, and K. Yamauchi, Experimental consideration of multistage martensitic transformation and precipitation behavior in aged Ni-rich Ti-Ni shape memory alloys, Mater. Trans. **44**, 2631 (2003).

[35] S. Kustov, B. Mas, D. Salas, E. Cesari, S. Raufov, V. Nikolaev, and J. Van Humbeeck, On the effect of room temperature ageing of Ni-rich Ni–Ti alloys, Scr. Mater. **103**, 10 (2015).

[36] P. C. Chang, M. L. Ko, B. Ramachandran, Y. K. Kuo, C. Chien, and S. K. Wu, Comparative study of R-phase martensitic transformations in TiNi-based shape memory alloys induced by point defects and precipitates, Intermetallics **84**, 130 (2017).

[37] J. Uchil, K. G. Kumara, and K. K. Mahesh, Effect of thermal cycling on R-phase stability in a NiTi shape memory alloy, Mater. Sci. Eng. A **332**, 25 (2002).

[38] X. Wang, S. Kustov, K. Li, D. Schryvers, B. Verlindena, and J. V. Humbeeck, Effect of nanoprecipitates on the transformation behavior and functional properties of a Ti-50.8 at.% Ni alloy with micron-sized grains, Acta Mater. **82**, 224 (2015).

[39] C. Chien, C. S. Tsao, S. K. Wu, C. Y. Chang, P. C. Chang, and Y. K. Kuo, Characteristics of the strain glass transition in as-quenched and 250 °C, early-aged $Ti_{48.7}Ni_{51.3}$ shape memory alloy, Acta Mater. **120**, 159 (2016).

[40] P. Filip and K. Mazanec, On precipitation kinetics in TiNi shape memory alloys, Scr. Mater. **45**, 701 (2001).

[41] J. Khalil-Allafi, A. Dlouhy, and G. Eggeler, Ni_4Ti_3-precipitation during aging of NiTi shape memory alloys and its influence on martensitic phase transformations, Acta Mater. **50**, 4255 (2002).

[42] D. Xue, Y. Zhou, and X. Ren, The effect of aging on the B2-R transformation behaviors in Ti-51 at % Ni alloy, Intermetallics **19**, 1752 (2011).

[43] Y. Ji, X. Ding, T. Lookman, K. Otsuka, and X. Ren, Heterogeneities and strain glass behavior: Role of nanoscale precipitates in low-temperature-aged $Ti_{48.7}Ni_{51.3}$ alloys, Phys. Rev. B **87**, 104110 (2013).

[44] G. L. Zhao and B. N. Harmon, Electron-phonon interactions and the phonon anomaly in β-phase NiTi, Phys. Rev. B **48**, 2031 (1993).

[45] J. G. Niu and W. T. Geng, Anti-precursor effect of Fe on martensitic transformation in TiNi alloys, Acta Mater. **104**, 18 (2016).

[46] Y. C. Lai and S. K. Wu, A study on phase transformation exhibited in $Ti_{49\pm x}Ni_{49\pm x}Fe_2$ ($x = 0$ to 1) shape memory alloys, Metall. Mater. Trans. A **52**, 4636 (2021).

[47] C. H. Tu, S. K. Wu, C. Lin, and B. Y. Huang, A study on two R-phase transformations in intermediate temperature aged Ni-rich TiNiFe-based shape memory alloys, Intermetallics **132**, 107123 (2021).

[48] P. Bag, Y. C. Su, Y. K. Kuo, Y. C. Lai, and S. K. Wu, Physical properties of face-centered cubic structured high-entropy alloys: Effects of NiCo, NiFe, and NiCoFe alloying with Mn, Cr, and Pd, Phys. Rev. Mater. **5**, 085003 (2021).

[49] S. Kustov, D. Salas, E. Cesari, R. Santamarta, D. Mari, and J. Van Humbeeck, Structural anelasticity, elasticity and broken ergodicity in Ni-Ti shape memory alloys, Acta Mater. **73**, 275 (2014).

[50] B. D. Ingale, W. C. Wei, P. C. Cheng, Y. K. Kuo, and S. K. Wu, Anomalous transport and thermal properties of NiTi and with Cu and Fe-doped shape memory alloys near the martensitic transition, J. Appl. Phys. **110**, 113721 (2011).

[51] Y. Zhou, J. Zhang, G. Fan, X. Ding, J. Sun, X. Ren, and K. Otsuka, Origin of 2-stage R-phase transformation in low-temperature aged Ni-rich Ti–Ni alloys, Acta Mater. **53**, 5365 (2005).

[52] G. Fan, W. Chen, S. Yang, J. Zhu, X. Ren, and K. Otsuka, Origin of abnormal multistage martensitic transformation behavior in aged Ni-rich Ti-Ni shape memory alloys, Acta Mater. **52**, 4351 (2004).

[53] S. K. Satija, S. M. Shapiro, M. B. Salamon, and C. M. Wayman, Phonon softening in $Ni_{46.8}Ti_{50}Fe_3$, Phys. Rev. B **29**, 6031 (1984).

[54] S. K. Wu and H. C. Lin, The effect of precipitation hardening on the MS temperature in a $Ti_{49.2}Ni_{50.8}$ alloy, Scr. Mater. **25**, 1529 (1991).

[55] M. E. Manley, M. Asta, J. C. Lashley, C. M. Retford, W. L. Hults, R. D. Taylor, D. J. Thomas, J. L. Smith, R. E. Hackenberg, and K. Littrell, Soft-phonon feature, site defects, and a frustrated phase transition in $Ni_{50}Ti_{47}Fe_3$: Experiments and first-principles calculations, Phys. Rev. B **77**, 024201 (2008).

[56] X. Ren, N. Miura, J. Zhang, K. Otsuka, K. Tanaka, M. Koiwa, T. Suzuki, Yu. I. Chumlyakov, and M. Asai, A comparative study of elastic constants of Ti-Ni-based alloys prior to martensitic transformation, Mater. Sci. Eng. A **312**, 196 (2001).